

SCIENTIFIC REPORTS

OPEN

Effect of Surface Defect States on Valence Band and Charge Separation and Transfer Efficiency

Juan Xu^{1,2,3}, Yiran Teng^{1,2,3} & Fei Teng^{1,2,3,4,5}

Received: 17 May 2016

Accepted: 09 August 2016

Published: 02 September 2016

Both energy band and charge separation and transfer are the crucial affecting factor for a photochemical reaction. Herein, the BiOCl nanosheets without and with surface bismuth vacancy (BOC, V-BOC) are prepared by a simple hydrothermal method. It is found that the new surface defect states caused by bismuth vacancy have greatly up-shifted the valence band and efficiently enhanced the separation and transfer rates of photogenerated electron and hole. It is amazing that the photocatalytic activity of V-BOC is 13.6 times higher than that of BOC for the degradation methyl orange (MO). We can develop an efficient photocatalyst by the introduction of defects.

As a green advanced oxidation technology, solar energy-driven photocatalysis has attracted much attention¹. However, its practical applications are still limited by low quantum efficiency, light utilization efficiency and photoactivity. Thus, it remains a big challenge to develop inexpensive, highly efficient photocatalysts for the practical applications.

Recently, considerable attention has been paid to the BiOCl photocatalyst, due to its exceptional optical and electronic properties, nontoxicity, low cost and high photocatalytic activity^{2–5}. Due to a wide band gap (3.19–3.60 eV), nevertheless, BiOCl can only absorb ultraviolet light, which is merely about 3–5% of solar energy⁶. Consequently, many attempts have been made to solve the problem, for example, morphology control⁷, heterojunction^{8–16}, doping with metal or non-metal¹⁷, etc. In the latter case, however, the bulk defects introduced by dopants can act as the recombination centres of electron-hole pairs, resulting in the decrease of photoactivity¹⁸. Compared with bulk defects, surface defects as charge traps can prevent the electron-hole recombination, thus contributing to the improvement of photocatalytic activity^{19,20}. The effect of oxygen vacancies on photoactivity has also been widely reported by researchers^{21–27}. For example, Zhu *et al.* have demonstrated that the introductions of surface oxygen vacancies in ZnO and BiPO₄ are conducive to the narrowing of band gap and the improvements of photoactivity^{28–30}. Liu *et al.* investigated the effect of surface cation vacancy on the photocatalytic activity of CoSe₂ nanosheets³¹. Guan *et al.* have also reported the formation of triple Bi-O-Bi vacancy in BiOCl³². To the best of our knowledge, however, the effect of the BiOCl with surface bismuth defects on photoactivity has never been in detail reported so far.

Herein, we report the generation of surface bismuth defects of BiOCl nanosheets. It is amazing that the BiOCl nanosheets with surface bismuth defects (V-BOC) show an exceptionally higher photocatalytic activity, compared with the BiOCl nanosheets without surface bismuth defects (BOC). We have explored the essence relationship between surface bismuth defects and activity. This study may provide a new idea to develop efficient photocatalysts.

¹Jiangsu Engineering and Technology Research Center of Environmental Cleaning Materials (ECM), Nanjing University of Information Science & Technology, 219 Ningliu Road, Nanjing 210044, China. ²Jiangsu Collaborative Innovation Center of Atmospheric Environment and Equipment Technology (CICAET), Nanjing University of Information Science & Technology, 219 Ningliu Road, Nanjing 210044, China. ³School of Environmental Science and Engineering, Nanjing University of Information Science & Technology, 219 Ningliu Road, Nanjing 210044, China. ⁴Jiangsu Joint Laboratory of Atmospheric Pollution Control (APC), Nanjing University of Information Science & Technology, 219 Ningliu Road, Nanjing 210044, China. ⁵Jiangsu Key Laboratory of Atmospheric Environment Monitoring and Pollution Control (AEMPC), Nanjing University of Information Science & Technology, 219 Ningliu Road, Nanjing 210044, China. Correspondence and requests for materials should be addressed to F.T. (email: tfwd@163.com)

Sample	Bi atom%	O atom%	Cl atom%	Bi:O
BOC	22.588	29.923	23.572	0.75:1
V-BOC	21.426	29.694	23.108	0.72:1

Table 1. XPS surface element analysis of the BOC and V-BOC samples.

Sample	Bi atom%	O atom%	Cl atom%	Bi:O
BOC	24.783	29.156	29.026	0.85:1
V-BOC	23.866	29.385	31.866	0.81:1

Table 2. Elemental composition of the BOC and V-BOC samples by inductively coupled plasma mass spectrometry (ICP-MS).

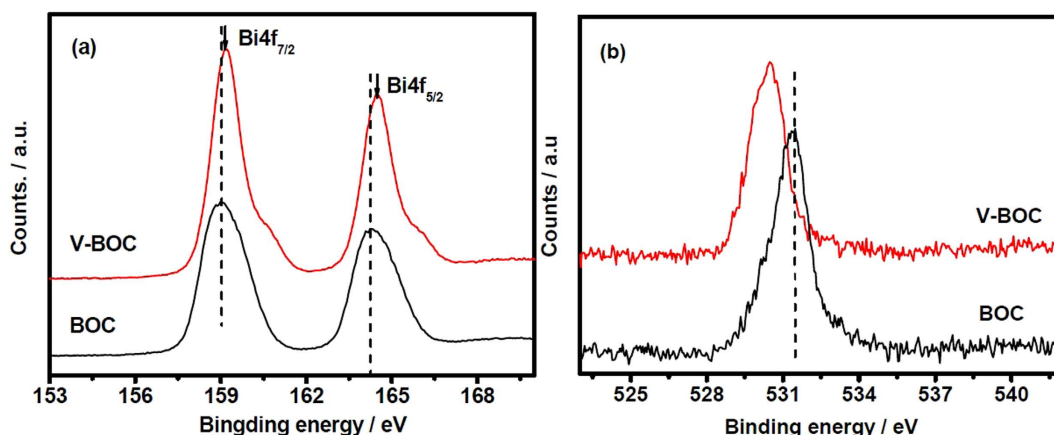


Figure 1. (a) Bi 4f and (b) O 1s photoelectron spectra for the BOC and V-BOC samples.

Results and discussion

Crystal structure of BOC and V-BOC. The crystalline structures of the BOC and V-BOC samples are determined by X-ray diffraction (XRD) (Figure S1, Seeing electronic supporting information, (ESI[†])). All the diffraction peaks of both samples can be well indexed to the tetragonal phase of BiOCl with the cell constants of $a = 3.891 \text{ \AA}$, $c = 7.369 \text{ \AA}$ (JCPDS No. 06-0249), which has a PbFCl^- -type structure with a space group of $P4/nmm$ ³³. No other impurities peaks are detected, indicating the formation of the phase-pure BiOCl. The layered BiOCl is constructed by the Cl ion layer and the bismuth-oxygen (Bi-O) layer.

Figure S2 (ESI[†]) shows the scanning electron microscopy (SEM) images of BOC and V-BOC samples. The BOC sample is composed of the microspheres with the diameters ranging from 4 to 7 μm (Figure S2a, ESI[†]). The microspheres are assembled by numerous nanosheets with $0.3 \mu\text{m} \times 0.5 \mu\text{m} \times 0.2 \mu\text{m}$ (Figure S2b, ESI[†]), which is similar to our previous report³⁴. The V-BOC sample (Figure S2c,d, ESI[†]) is composed of the nanosheets of $1.5 \mu\text{m} \times 1 \mu\text{m} \times 0.2 \mu\text{m}$. Their high-resolution transmission electron microscopy (HRTEM) images are shown in Figure S3 (ESI[†]) to clearly prove the presence of the defect shell. For BOC and V-BOC samples, the lattice fringe spacing is 0.34 nm, corresponding to the (101) plane of BiOCl. Compared with Figure S3a (ESI[†]), we can see that the thickness of defect shell is about 5.51 nm from Figure S3b (ESI[†]), and the lattice fringes of V-BOC become indiscernible indicated by red circle (Figure S3c,d, ESI[†]). This indicates that the defects exist everywhere in the V-BOC sample.

XPS, ICP and FT-IR spectra. To further understand the defect structure, the XPS surface elements analysis is performed to detect the Bi and O atoms in both BiOCl samples. In Table 1, the atom ratio of Bi to O is 0.72 for the V-BOC sample, which is slightly lower than that (0.75) of BOC. Moreover, the inductively coupled plasma mass spectrometry (ICP-MS) has been performed to detect the Bi and O in both BiOCl samples. The ICP-MS results (Table 2) show that the Bi/O ratio in BOC and V-BOC are 0.85 and 0.81, respectively. This also suggests that the bismuth vacancies are generated in the V-BOC sample. As a surface analysis method, the XPS analysis is mainly focused on the surface atoms layer with the depth about 2–5 nm for inorganic semiconductor materials, which fits well thickness of defect shell (Figure S3, ESI[†]). The survey XPS spectra of both samples are shown in Figure S4 (ESI[†]). We can observe that the elements present are Bi, O, C and Cl, the peak at 284.8 eV could be readily assigned to the binding energies of C 1s (Figure S4, ESI[†]), which results from the adventitious carbon on the sample surface that is nearly unavoidable. This also indicates the formation of the pure BiOCl. Figure 1 shows their Bi 4f and O 1s peaks. Compared with BOC, the Bi 4f peaks of V-BOC shift to a higher binding energy (Fig. 1a). Furthermore, the binding energy of O 1s is about 530.4 eV for V-BOC, which is smaller than that (531.5 eV) of BOC (Fig. 1b). This shift may be attributed to the weakened hybridization between Bi 6s and

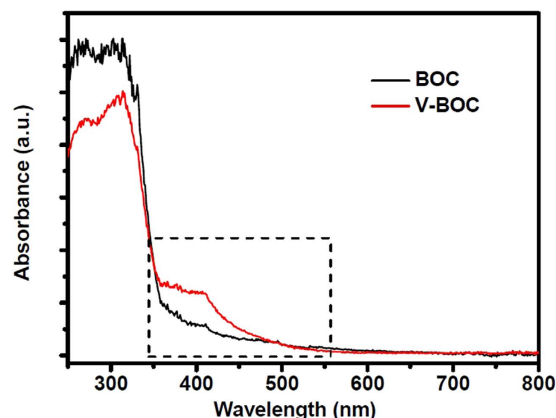


Figure 2. UV-vis diffuse reflectance spectra (UV-DRS) of the BOC and V-BOC samples.

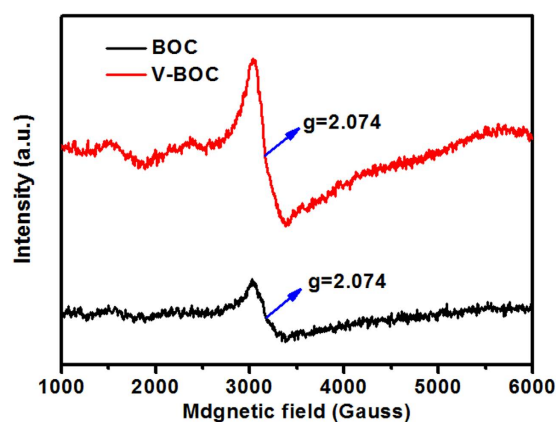


Figure 3. EPR spectra of the BOC and V-BOC samples.

O 2p, which leads to the decrease of binding energy of bismuth-oxygen bond (Bi-O)³⁰. These shifts indicate the formation surface bismuth defects or oxygen vacancies in the V-BOC³⁵. From Table 1 and Table 2, we can see the O atom of V-BOC is the same with the BiOCl. So the formation of defect in the V-BOC sample is attributed to the lack of Bi element. The same phenomenon has occurred in Bi₆S₂O₁₅ system³⁰, in which they have reported that the generation of surface bismuth defects resulted in a lower binding energy³⁰.

The Fourier transform infrared (FT-IR) spectra show the characteristic absorption peaks of these two samples (Figure S5, ESI[†]). The absorption bands at 1400 cm⁻¹ could be assigned to the asymmetry and symmetric stretching vibrations of Bi-Cl band, while the absorption bands at 522 cm⁻¹ are assigned to the Bi-O stretching vibrations³⁶. The bands at 3455 and 1623 cm⁻¹ are the stretching and flexural vibrations of O-H for adsorbed water molecules, respectively³⁶. The bands at 2927 and 1043 cm⁻¹ stem from the stretching vibrations of C-H and C-O-C bonds, respectively; which are originated from ethylene glycol molecules adsorbed on the surface of the samples³⁷. No significant change in FT-IR spectra can be found for both samples, indicating that the crystal structure does not change, which is in good agreement with the XRD results.

Optical property. Figure 2 displays the ultraviolet-visible diffuse reflection spectra (UV-DRS) of both samples. It is interesting that the UV-DRS spectral response of V-BOC sample is greatly expanded and enhanced because of the introduction of surface bismuth vacancy. The absorption edge of BOC is about 381.5 nm, corresponding to the band gap of 3.25 eV. In comparison, the main absorption edge and the highest absorption peak of V-BOC nanosheets do not change ($\lambda < 355$ nm). However, its absorbance is enhanced obviously in the range 350–500 nm, the band gap of the V-BOC nanosheets is ~2.91 eV, which may be caused by surface bismuth vacancy, as it does in Bi₆S₂O₁₅³⁰. The improved optical absorption is expected to contribute to the improvement of photocatalytic activity.

EPR spectra. Moreover, electron paramagnetic resonance (EPR) of the as-prepared samples has been performed (Fig. 3). EPR is a sensitive and direct technology to monitor surface defect behaviors of material. From Fig. 3, it can be found that for V-BOC, the intensity of the EPR signal at g factor of ~2.074 is much higher than that of BOC. The peak at $g = \sim 2.1$ has been reported previously to be the surface bismuth defects³⁸. This result

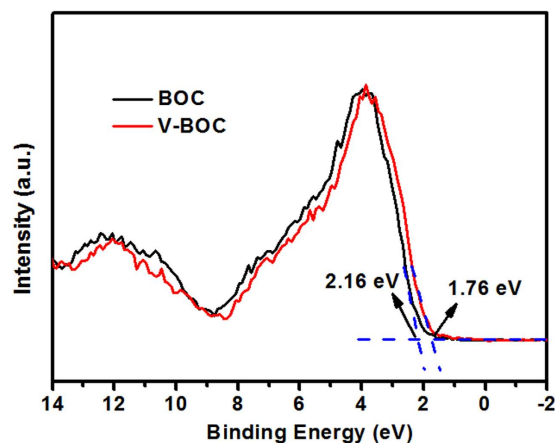


Figure 4. Valence-band XPS spectra of the BOC and V-BOC samples.

is consistent with the valence band based X-ray photoelectron spectroscopy (XPS) analysis. Both XPS and EPR results demonstrate the presence of the surface Bi vacancy in V-BOC.

Valence band based XPS and Mott-schottky plots. The UV-DRS (Fig. 2) reveals that the band gap of the V-BOC nanosheets is ~ 2.91 eV, smaller than that (3.25 eV) of BOC, which can be attributed to the existence of surface bismuth defects.

Further, the valence bands (VB) of both BOC and V-BOC are measured by the valence band X-ray photoelectron spectroscopy (XPS) to confirm the energy band positions, as shown in Fig. 4. BOC displays a VB with the edge of the maximum energy at about 2.16 eV. Combining the test results of UV-DRS (Fig. 2), the CB minimum energy is -1.09 eV. For V-BOC, however, the VB maximum energy up shifts to 1.76 eV, compared with that of BOC. Combined with the results of UV-DRS (Fig. 2), the CB minimum of V-BOC occurs at -1.15 eV and shifts up by 0.06 eV, compared with that of BOC. According to the results above, the introduction of surface bismuth vacancies in our research elevated whole bands and many shallow surface bismuth-vacancy states appear above and partly overlapping with the VB. And the valence-band maximum (VBM) of V-BOC is raised by 0.4 eV. We could draw a conclusion that the VB width was widened due to the presence of the surface Bi vacancy.

Furthermore, the Mott-Schottky plots are also tested to confirm the energy band positions, the CB bottoms of BOC and V-BOC can be estimated by the Mott-Schottky plots. It can be calculated through the following Equation (1):

$$\Delta E = E_{CB} - E_{fb} \quad (1)$$

where E_{fb} is the flat-band potential, E_{CB} is the conduction band potential. Herein, ΔE is assumed to be -0.3 V for the n -type semiconductor. As shown in Figure S6, the E_{fb} are -0.37 and -0.84 V vs. SCE for BOC and V-BOC, respectively. As a result, the CB potential of V-BOC is about -1.14 V vs. SCE, which is higher than that (-0.67 V vs. SCE) of BOC. Combining with the determined band gap by UV-DRS, the oxidation potentials of VB are estimated to be 2.58 and 1.77 V vs. SCE for BOC and V-BOC, respectively.

Photochemical properties. Their photocatalytic activities are evaluated by the degradation of methyl orange (MO) under visible light ($\lambda > 420$ nm) and UV light irradiation ($\lambda \leq 420$ nm). Although the V-BOC can absorb visible light, MO can not be degraded under visible light ($\lambda > 420$ nm) (Figure S7, ESI[†]). As shown in Fig. 5a, it is clear that the V-BOC shows a greatly higher photocatalytic activity than BOC. The apparent reaction rate constants are determined to be 0.00409 and 0.05566 min^{-1} for BOC and V-BOC, respectively (Fig. 5b). The photocatalytic activity of V-BOC is about 13.6 times as high as that of BOC. Further, we have carried out cycling experiments to investigate the stability of V-BOC (Figure S8, ESI[†]). The photocatalytic activity of V-BOC does not decrease after 4 cycles, demonstrating that the V-BOC photocatalyst is stable.

It is well known that the photocatalytic activity of photocatalyst is affected by various factors, such as crystal structure, particle morphology, surface area, band gap, separation and transfer efficiency of charges, and so on^{39,40}. First, the crystal phases are same for both samples. Second, the BOC sample is composed of the microspheres with the diameters ranging from 4 to 7 μm , and the microspheres are made up of numerous nanosheets with the size of $0.3 \mu\text{m} \times 0.5 \mu\text{m} \times 0.2 \mu\text{m}$. The size of BOC nanosheets is much smaller than that ($1.5 \mu\text{m} \times 1 \mu\text{m} \times 0.2 \mu\text{m}$) of V-BOC. Moreover, the BET area ($15.9 \text{ m}^2 \text{ g}^{-1}$) of the BOC sample is much larger than that ($4.3 \text{ m}^2 \text{ g}^{-1}$) of V-BOC sample. On base of BET areas, the BOC should have a higher activity for the degradation of MO than that of V-BOC. However, the actual test result is that V-BOC has a greatly higher activity than BOC, indicating that the particle morphology is not the main factor. The results imply the enhanced activity of V-BOC has nothing to do with these two factors. Third, the separation and transfer efficiency of electron-hole pairs are investigated by the electrochemical impedance spectra (EIS)⁴¹. In Figure S9a (ESI[†]), the arc radius of V-BOC is smaller than that of BOC. A smaller semicircle radius in EIS Nyquist plot means a smaller electric resistance of electrode, thus the former has a higher electron transfer ability than the latter.

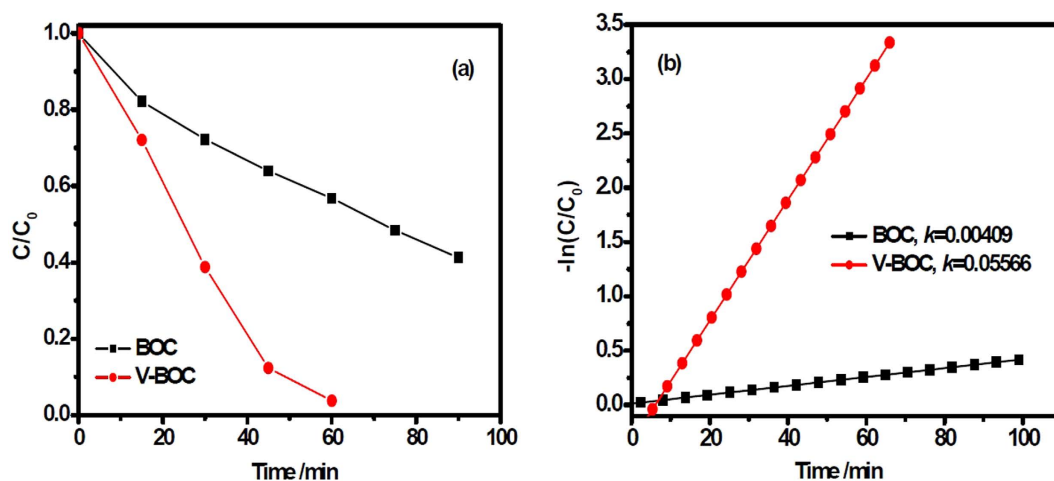


Figure 5. (a) Degradation curves and (b) reaction kinetic curves of MO over the BOC and V-BOC samples under UV light irradiation ($\lambda \leq 420$ nm).

PL and photocurrent spectra. Moreover, the separation efficiency of the photo-generated electrons and holes can be investigated by photoluminescence (PL)⁴². Figure S9b (ESI^T) shows their PL spectra under the excitation wavelength of 381 nm. Both samples show the intrinsic fluorescence emission peaks at around 381 nm. The peak intensity of the V-BOC is lower than that of BOC. Generally, a low PL emission intensity indicates a low recombination efficiency of photogenerated charges, leading to a high photocatalytic activity.

Further, from Figure S9c (ESI^T) shows the photocurrent response spectra at each switch-on and switch-off event for both electrodes, in which the photocurrent response of V-BOC is higher than that of BOC. The result is in accord with the photocatalytic activity order. The higher photocurrent response of V-BOC indicates the improved separation efficiency of photoinduced electron-hole pairs, which could be caused by the induction of the surface bismuth vacancy. We assume that the surface bismuth vacancy, like conventional oxygen vacancy³⁷, may serve as the carrier trap to prevent the electrons and holes recombination. Summarily, it is the surface bismuth vacancy with higher electronic conductivity that improves the charge separation efficiency, eventually enhancing the photocatalytic activity.

Trapping experiments. To further elucidate the photocatalytic mechanism, the trapping experiments are performed to detect the main oxidative species (radicals or holes) in the photocatalytic process, in which $(\text{NH}_4)_2\text{C}_2\text{O}_4 \cdot \text{H}_2\text{O}$ as hole scavenger and isopropyl alcohol (IPA) as hydroxyl radical scavenger are added to the reaction system during the degradation of MO, respectively (Figure S10, ESI^T). In both BOC- and V-BOC-containing reaction systems, the degradation activities of MO are both greatly reduced while adding $(\text{NH}_4)_2\text{C}_2\text{O}_4 \cdot \text{H}_2\text{O}$. On the contrary, the addition of IPA only causes a small change in the degradation of MO. Thus, the results suggest that the holes are the main oxidative species in both systems.

Role of surface vacancy states. On Base of the results above, we have proposed a schematic diagram to describe the energy band position variation of V-BOC (Fig. 6a). Also, a mechanism of charge separation and photocatalytic reaction of V-BOC is shown in Fig. 6. The forbidden band of BiOCl is wide (about 3.25 eV), which can only be excited by UV light with the wavelengths shorter than 381.5 nm. After surface bismuth vacancies are introduced, however, the shallow surface bismuth-vacancy states (SBv. states) are generated, one part of which locates above, and another part of which overlaps with the VB of BiOCl. This would narrow the band gap, thus expanding the photo-response wavelength to 426.1 nm (about 2.91 eV). Although the V-BOC can absorb visible light, MO cannot be degraded under visible light ($\lambda > 420$ nm). We assume that the vacancy mainly contribute to the improvement of separation and transport efficiency of electron-hole pairs. The similar results have also been reported previously by Sun *et al.*²¹ and Zhu *et al.*³⁰ The VB width was widened due to the presence of the surface Bi vacancy. Guan *et al.*³² and Liu *et al.*⁴³ have demonstrated that the increased VB width is beneficial for the separation of charge carriers, because the VB width intrinsically controls the mobility of holes: the wider the VB is, the higher the mobility of holes generated is^{32,43}. The VB width not only makes the better photo-oxidation of holes, but also promotes the transfer of photoexcited electrons to reactants, favoring for the inhibition of the electron-hole recombination^{32,43}. Thus the widened VB width can improve the separation and transport of electron-hole pairs.

On base of the energy band structure (Fig. 6b), we assume that O_2 can be reduced to $\cdot\text{O}_2^-$ by the photo-generated electrons, which could further transform to H_2O_2 via $\cdot\text{O}_2^- + \text{e} + 2\text{H}^+ \rightarrow \text{H}_2\text{O}_2$ ⁴⁴. Besides, H_2O is oxidized to $\cdot\text{OH}$ by the photogenerated holes. The formed $\cdot\text{OH}$ and holes are strong oxidants for dye molecules. Our results above have confirmed that holes are the main oxidative species, so the MO dye can be easily decomposed.

Summarily, the SBv. states by surface bismuth vacancy can not only narrow the band gap, but also widen the VB width, which contributes to the increase of light absorption range and the improvement of separation and

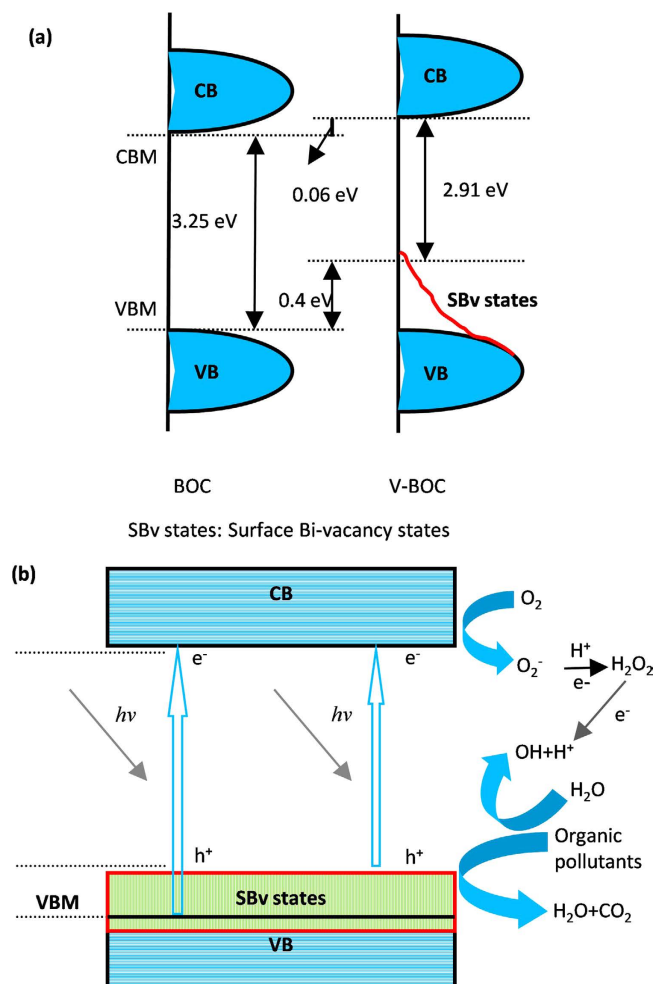


Figure 6. Schematic diagram of (a) the positions of VB and CB of BOC and V-BOC; (b) the reaction mechanism over BOC and V-BOC under UV light irradiation ($\lambda \leq 420$ nm).

transport efficiency of photoinduced electron-hole pairs, thus the photocatalytic activity can be improved by surface bismuth vacancy.

Conclusions

To conclude, the surface bismuth vacancies have greatly up shifted the valence band (VB), and narrowed the band gap of V-BOC. Thus, the photocatalytic activity of V-BOC has been greatly improved. This work provides us with a powerful strategy to develop a highly-efficient photocatalyst.

Methods

All reagents were of analytical grade, purchased from Beijing Chemical Reagents Industrial Company of China, and were used without further purification.

Synthesis of BiOCl nanosheets without surface bismuth vacancy (BOC). The BiOCl nanosheets without surface bismuth vacancy (BOC) was prepared according to previously reported method³⁴. In detail, 1.5 mmol of $Bi(NO_3)_3 \cdot 5H_2O$ was dissolved in 30 mL of ethylene glycol (EG) under stirring at room temperature. After the $Bi(NO_3)_3 \cdot 5H_2O$ was completely dissolved, 10 mmol of NaCl was added to the above solution. After stirring for 30 min, the solution was transferred into a 50-mL Teflonlined stainless steel autoclave, and then maintained at 170 °C for 6 h. After reaction, the autoclave was cooled to room temperature naturally. The resulting precipitate was centrifuged and washed with ethanol and distilled water three times, and then dried at 60 °C for 3 h.

Synthesis of BiOCl nanosheets with surface bismuth vacancy (V-BOC). In a typical procedure, 0.5 mmol Bi_2O_3 and 8 mmol NH_4Cl (1:16 molar ratio) were mixed together, and then 20 mL of H_2O_2 was added. The resulting precursor suspension was magnetically stirred for 30 min at room temperature and then transferred into 50-mL Teflon-lined stainless steel autoclave, and then maintained at 180 °C for 12 h. After reaction, the autoclave was cooled to room temperature naturally. The resulting precipitate was centrifuged and washed with ethanol and distilled water three times, and then dried at 60 °C for 3 h.

Sample characterizations. The crystal structures of the samples were determined by X-ray powder polycrystalline diffractometer (Rigaku D/max-2550 VB), using graphite monochromatized Cu K radiation ($\lambda = 0.154 \text{ nm}$), operating at 40 kV and 50 mA. The XRD patterns were obtained in the range of $20\text{--}80^\circ$ (2θ) at a scanning rate of 7° min^{-1} . The samples were characterized on a scanning electron microscope (SEM, Hitachi SU-1510) with an acceleration voltage of 15 keV. The samples were coated with 5-nm-thick gold layer before observations. The fine surface structures of the samples were determined by high-resolution transmission electron microscopy (HRTEM, JEOL JEM-2100F) equipped with an electron diffraction (ED) attachment with an acceleration voltage of 200 kV. Nitrogen sorption isotherms were performed at 77 K and $<10^{-4}$ bar on a Micromeritics ASAP2010 gas adsorption analyzer. Each sample was degassed at 150°C for 5 h before measurements. Surface area was calculated by the Brunauer-Emmett-Teller (BET) method. Fourier transform infrared spectra (FT-IR) were recorded on a Fourier transform infrared spectra (FT-IR, KBr disk method; Thermo Scientific Nicolet iS5) at the wavenumber range of $400\text{--}4000 \text{ cm}^{-1}$.

X-ray photoelectron spectroscopy (XPS) measurements were done on a VG ESCALAB MKII XPS system with Mg K_α source and a charge neutralizer. All the binding energies were referenced to the C1s peak at 284.8 eV of the surface adventitious carbon. The electron paramagnetic resonance (EPR) spectra were collected using a Bruker ESP 500 spectrometer at 90 K. UV-vis diffused reflectance spectra (UV-DRS) of the samples were obtained using a UV-vis spectrophotometer (UV-2550, Shimadzu, Japan). BaSO_4 was used as a reflectance standard in a UV-vis diffuse reflectance experiment. The valence band based X-ray photoelectron spectroscopy (XPS) was performed to estimate the VB position of the as-prepared samples through a PHI 5300 ESCA system. The photoluminescence (PL) spectra were obtained on Cary Eclipse fluorescence spectrophotometer at room temperature. The PL lifetime was measured using time-resolved fluorescence decay spectra by time-correlated single-photon counting under the 260 nm laser excitation (Cary Eclipse, Agilent). The Mott-Schottky method was applied to measure the flat potential (E_{fb}) of semiconductor particle films, which are immersed in $0.1 \text{ mol L}^{-1} \text{ Na}_2\text{SO}_4$ solution ($\text{pH} = 7$), which is carried out in conventional three electrode cells using a CHI660D electrochemical workstation (Shanghai Chenhua Instrument Co., Ltd., Shanghai, China).

Measurements of photocurrents and EIS. An electrochemical system (CHI-660B, China) was employed to measure the photocurrents and electrochemical impedance spectroscopy (EIS). Electrochemical impedance spectroscopy (EIS) was performed from 0.1 Hz to 100 kHz at an open circuit potential of 0.3 V and an alternating current (AC) voltage amplitude of 5 mV. The data were analyzed by ZSimWin software. Photocurrent measurements were carried out in a conventional three-electrode system, in which indium-tin oxide (ITO) glass was used as the current collector to fabricate photo electrode, and $0.1 \text{ M Na}_2\text{SO}_4$ was used as the electrolyte solution. BOC/ITO and V-BOC/ITO photo electrode were prepared by a coating method. Potentials were given with reference to the standard calomel electrode (SCE).

Evaluation of photo catalytic activity. The photo catalytic activity of the sample was evaluated by the degradation of methyl orange (MO) aqueous solution under UV light ($\lambda \leq 420 \text{ nm}$), using a 300 W Xe arc lamp (CEL-HXF 300) equipped with an ultraviolet cutoff filter as a light source. The reaction system was placed in a sealed black box with the top opened, and was maintained a distance of 15 cm from the light source. The photocatalysts (100 mg) were dispersed in 200 mL of 10 mg/L MO aqueous solution in a Pyrex beaker at room temperature. Before lighting on, the suspension was continuously stirred for 30 min in the dark to ensure the establishment of an adsorption-desorption equilibrium between the catalysts and MO solution. During degradation, 3 mL of solution was collected by pipette at an interval of irradiation, and subsequently centrifuged to remove the catalysts. UV-vis absorption spectra were recorded on a Spectrumbab 722sp spectrophotometer to determine the concentration of MO. The degradation reaction could be expressed by an apparent first-order rate constant (k_a), which could be calculated using the following Equation (2):

$$\ln(C_0/C) = k_a \times t, \text{ or } C = C_0 \times \exp(-k_a \times t) \quad (2)$$

where C_0 is the initial concentration of MO solution, and C is the concentration of MO at t -min irradiation, respectively. The active species generated in the photocatalytic reaction were detected through trapping experiments, in which 0.25 mmol isopropanol (IPA) and 1 mmol ammonium oxalate ($(\text{NH}_4)_2\text{C}_2\text{O}_4$) were used as hydroxyl radicals scavenger and holes scavenger, respectively.

References

1. Linford, M. R., Auch, M. & Mohwald, H. Nonmonotonic effect of ionic strength on surface dye extraction during dye-polyelectrolyte multilayer formation. *J. Am. Chem. Soc.* **120**, 178–182 (1998).
2. Ma, J. M., Liu, X. D., Lian, J. B., Duan, X. C. & Zheng, W. J. Ionothermal synthesis of BiOCl nanostructures via a long-chain ionic liquid precursor route. *Cryst. Growth & Des.* **10**, 2522–2527 (2010).
3. Li, K. Photocatalytic fuel cell (PFC) and dye self-photosensitization photocatalytic fuel cell (DSPFC) with BiOCl/Ti photoanode under UV and visible light irradiation. *Environ. Sci. Technol.* **47**, 3490–3497 (2013).
4. Peng, H. L., Chan, C. K., Meister, S., Zhang, X. F. & Cui, Y. Shape evolution of layer-structured bismuth oxychloride nanostructures via low-temperature chemical vapor transport. *Chem. Mater.* **21**, 247–252 (2008).
5. Zhang, K. *et al.* BiOCl sub-microcrystals induced by citric acid and their high photocatalytic activities. *Cryst. Growth & Des.* **12**, 793–803 (2012).
6. Chakraborty, A. K., Rawal, S. B., Han, S. Y., Chai, S. Y. & Lee, W. I. Enhancement of visible-light photocatalytic efficiency of BiOCl/ Bi_2O_3 by surface modification with WO_3 . *Appl. Catal. A* **407**, 217–223 (2011).
7. Weng, S. X. Construction of toothlike homojunction BiOCl (001) nanosheets by selective etching and its high photocatalytic activity. *ACS Appl. Mater. Interfaces* **6**, 18423–18428 (2014).
8. Chai, S. Y. Heterojunctioned BiOCl/ Bi_2O_3 , a new visible light photocatalyst. *J. Catal.* **262**, 144–149 (2009).
9. Wang, Q. Z. Photodegradation of methyl orange with PANI-modified BiOCl photocatalyst under visible light irradiation. *Appl. Surf. Sci.* **283**, 577–583 (2013).

10. Li, T. B. *et al.* New photocatalyst BiOCl/BiOI composites with highly enhanced visible light photocatalytic performances. *Dalton Trans.* **40**, 6751–6758 (2011).
11. Shamailla, S., Sajjad, A. K. L., Chen, F. & Zhang, J. L. WO₃/BiOCl, a novel heterojunction as visible light photocatalyst. *J. Colloid Interface Sci.* **356**, 465–472 (2011).
12. Chang, X. F. Enhancement of photocatalytic activity over NaBiO₃/BiOCl composite prepared by an *in situ* formation strategy. *Catal. Today*. **153**, 193–199 (2010).
13. Zhang, J. *et al.* Improvement of visible light photocatalytic activity over flower-like BiOCl/BiOBr microspheres synthesized by reactable ionic liquids. *Colloids Surf. A*. **420**, 89–95 (2013).
14. Cao, J., Xu, B. Y., Lin, H. L., Luo, B. D. & Chen, S. F. Novel Bi₂S₃-sensitized BiOCl with highly visible light photocatalytic activity for the removal of rhodamine B. *Catal. Commun.* **26**, 204–208 (2012).
15. Cheng, H. F., Huang, B. B., Qin, X. Y., Zhang, X. Y. & Dai, Y. A controlled anion exchange strategy to synthesize Bi₂S₃ nanocrystals/BiOCl hybrid architectures with efficient visible light photoactivity. *Chem. Commun.* **48**, 97–99 (2012).
16. Wang, C. D., Qiu, H., Inoue, T. & Yao, Q. W. Electronic structure calculations of I and Mn doped BiOCl with modified Becke–Johnson potential. *Comp. Mater. Sci.* **85**, 138–141 (2014).
17. Choi, W., Termin, A. & Hoffmann, M. R. The role of metal ion dopants in quantum-sized TiO₂: correlation between photoreactivity and charge carrier recombination dynamics. *J. Phys. Chem.* **98**, 13669–13679 (1994).
18. Kong, M. *et al.* Tuning the relative concentration ratio of bulk defects to surface defects in TiO₂ nanocrystals leads to high photocatalytic efficiency. *J. Am. Chem. Soc.* **133**, 16414–16417 (2011).
19. Chen, H. & Selloni, A. Surface and subsurface oxygen vacancies in anatase TiO₂ and differences with rutile. *Phys. Rev. B*. **79**, 092101 (2009).
20. Lv, Y. *et al.* Production of visible activity and UV performance enhancement of ZnO photocatalyst via vacuum deoxidation. *Appl. Catal. B*. **138**, 26–32 (2013).
21. Zhao, Z. *et al.* Effect of defects on photocatalytic activity of rutile TiO₂ nanorods. *Nano Res.* **8**, 4061–4071 (2015).
22. Naldoni, A. *et al.* Effect of nature and location of defects on bandgap narrowing in black TiO₂ nanoparticles. *J. Am. Chem. Soc.* **134**, 7600–7603 (2012).
23. Zhao, Z. *et al.* Reduced TiO₂ rutile nanorods with well-defined facets and their visible-light photocatalytic activity. *Chem. Commun.* **50**, 2755–2757 (2014).
24. Wang, G. M., Ling, Y. C. & Li, Y. Oxygen-deficient metal oxide nanostructures for photoelectrochemical water oxidation and other applications. *Nanoscale*. **4**, 6682–6691 (2012).
25. Diebold, U. The surface science of titanium dioxide. *Surf. Sci. Rep.* **48**, 53–229 (2003).
26. Chen, X. B., Liu, L. & Huang, F. Q. Black titanium dioxide (TiO₂) nanomaterials. *Chem. Soc. Rev.* **44**, 1861–1885 (2015).
27. Ling, Y. C. *et al.* The influence of oxygen content on the thermal activation of hematite nanowires. *Angew. Chem. Int. Ed.* **51**, 4074–4079 (2012).
28. Lv, Y. & Zhu, Y. Enhanced photocatalytic performance for the BiPO_{4-x} nanorod induced by surface oxygen vacancy. *J. Phys. Chem. C*. **117**, 18520–18528 (2013).
29. Lv, Y., Liu, Y. & Zhu, Y. Surface oxygen vacancy induced photocatalytic performance enhancement of a BiPO₄ nanorod. *J. Mater. Chem.* **2**, 1174–1182 (2014).
30. Wang, J., Jiang, W. J., Liu, D., Wei, Z. & Zhu, Y. F. Photocatalytic performance enhanced via surface bismuth vacancy of Bi₆S₂O₁₅ core/shell nanowires. *Appl. Catal. B*. **306**, 176–177 (2015).
31. Liu, Y. W. *et al.* Low overpotential in vacancy-rich ultrathin CoSe₂ nanosheets for water oxidation. *J. Am. Chem. Soc.* **136**, 15670–15675 (2014).
32. Guan, M. L. *et al.* Vacancy associates promoting solar-driven photocatalytic activity of ultrathin bismuth oxychloride nanosheets. *J. Am. Chem. Soc.* **135**, 10411–10417 (2013).
33. Bannister, F. A. The crystal structure of the bismuth oxyhalides. *Mineral. Mag.* **24**, 49–58 (1935).
34. Li, N. *et al.* *In situ* synthesis of uniform Fe₂O₃/BiOCl p/n heterojunctions and improved photodegradation properties for mixture dyes. *Dalton Trans.* **43**, 13742–13750 (2014).
35. Ye, L. Q. *et al.* Increasing visible-light absorption for photocatalysis with black BiOCl. *Phys. Chem. Chem. Phys.* **14**, 82–85 (2012).
36. Song, J. M., Mao, C. J., Niu, H. L., Shen, Y. H. & Zhang, S. Y. Hierarchical structured bismuth oxychlorides: self-assembly from nanoplates to nanoflowers via a solvothermal route and their photocatalytic properties. *Cryst Eng Comm.* **12**, 3875–3881 (2010).
37. Cheng, G., Xiong, J. Y. & Stadler, F. J. Facile template-free and fast refluxing synthesis of 3D desertrose-like BiOCl nanoarchitectures with superior photocatalytic activity. *New J. Chem.* **37**, 3207–3213 (2013).
38. Barreca, D., Morazzoni, F., Rizzi, G. A., Scotti, R. & Tondello, E. Molecular oxygen interaction with Bi₂O₃: a spectroscopic and spectromagnetic investigation. *Physical Chemistry Chemical Physics*. **3**, 1743–1749 (2001).
39. Zhu, S., Xu, T., Fu, H., Zhao, J. & Zhu, Y. Synergetic effect of Bi₂WO₆ photocatalyst with C₆₀ and enhanced photoactivity under visible irradiation. *Environ. Sci. Technol.* **41**, 6234–6239 (2007).
40. Pan, C., Li, D., Ma, X., Chen, Y. & Zhu, Y. Effects of distortion of PO₄ tetrahedron on the photocatalytic performances of BiPO₄. *Catal. Sci. Technol.* **1**, 1399–1405 (2011).
41. Hosseini, Z., Taghavinia, N., Sharifi, N., Chavoshi, M. & Rahman, M. Fabrication of high conductivity TiO₂/Ag fibrous electrode by the electrophoretic deposition method. *J. Phys. Chem. C*. **112**, 18686–18689 (2008).
42. Wang, Y., Wang, X. C. & Antonietti, M. Photocatalytic nanodiodes for visible-light photocatalysis. *Angew. Chem. Int. Ed.* **44**, 4585–4589 (2005).
43. Liu, G. *et al.* Unique electronic structure induced high photoreactivity of sulfur-doped graphitic C₃N₄. *J. Am. Chem. Soc.* **132**, 11642–11648 (2010).
44. Zhao, Y. B. *et al.* The Surface-structure sensitivity of dioxygen activation in the anatase-photocatalyzed oxidation reaction. *Angew. Chem., Int. Ed.* **124**, 3242–3246 (2012).

Acknowledgements

This work is financially supported by National Science Foundation of China (21377060), Scientific Research Foundation for the Returned Overseas Chinese Scholars of State Education Ministry (20121707), Six Talent Climax Foundation of Jiangsu (20100292), Natural Science Foundation of Jiangsu province (BK2012464), the Key Project of Environmental Protection Program of Jiangsu (2013005), the Project Funded by the Science and Technology Infrastructure Program of Jiangsu (BM201380277), and A Project Funded by the Priority Academic Program Development of Jiangsu Higher Education Institutions (PAPD) sponsored by SRF for ROCS, SEM (2013S002).

Author Contributions

J.X. performed the experiment and wrote the main text. Y.T. performed UV-DRS, EIS, SEM, HRTEM characterization, and made revision. F.T. designed the experiment, revised the paper and provided the financial support. All authors discussed the results and commented on the manuscript. All authors have reviewed the manuscript.

Additional Information

Supplementary information: accompanies this paper at <http://www.nature.com/srep>

Competing financial interests: The authors declare no competing financial interests.

How to cite this article: Xu, J. *et al.* Effect of Surface Defect States on Valence Band and Charge Separation and Transfer Efficiency. *Sci. Rep.* **6**, 32457; doi: 10.1038/srep32457 (2016).



This work is licensed under a Creative Commons Attribution 4.0 International License. The images or other third party material in this article are included in the article's Creative Commons license, unless indicated otherwise in the credit line; if the material is not included under the Creative Commons license, users will need to obtain permission from the license holder to reproduce the material. To view a copy of this license, visit <http://creativecommons.org/licenses/by/4.0/>

© The Author(s) 2016